

# The Equation of State and Some Key Parameters of Neutron Stars: Constraints from GW170817, the Nuclear Data, and the Low-mass X-ray Binary Data

JIN-LIANG JIANG,<sup>1,2</sup> SHAO-PENG TANG,<sup>1,2</sup> DONG-SHENG SHAO,<sup>1,2</sup> MING-ZHE HAN,<sup>1,2</sup> YIN-JIE LI,<sup>1,2</sup> YUAN-ZHU WANG,<sup>1</sup>  
ZHI-PING JIN,<sup>1,2</sup> YI-ZHONG FAN,<sup>1,2</sup> AND DA-MING WEI<sup>1,2</sup>

<sup>1</sup>*Key Laboratory of dark Matter and Space Astronomy, Purple Mountain Observatory, Chinese Academy of Sciences, Nanjing, 210023, China.*

<sup>2</sup>*School of Astronomy and Space Science, University of Science and Technology of China, Hefei, Anhui 230026, China.*

## ABSTRACT

In this work we parameterize the equation of state of dense neutron star (NS) matter with four pressure parameters of  $\{\hat{p}_1, \hat{p}_2, \hat{p}_3, \hat{p}_4\}$  and then set the combined constraints with the data of GW 170817 and the data of six low-mass X-ray binaries (LMXBs) with thermonuclear burst or alternatively the symmetry energy of the nuclear interaction. We find that the nuclear data effectively narrow down the possible range of  $\hat{p}_1$ , the gravitational-wave data plays the leading role in bounding  $\hat{p}_2$ , and the LMXB data as well as the lower bound on the maximal gravitational mass of non-rotating NSs govern the constraints on  $\hat{p}_3$  and  $\hat{p}_4$ . Using posterior samples of pressure parameters and some universal relations, we further investigate how the current data sets can advance our understanding of tidal deformability ( $\Lambda$ ), moment of inertia ( $I$ ), and binding energy (BE) of NSs. For a canonical mass of  $1.4M_\odot$ , we have  $I_{1.4} = 1.43^{+0.30}_{-0.13} \times 10^{38} \text{ kg} \cdot \text{m}^2$ ,  $\Lambda_{1.4} = 390^{+280}_{-210}$ ,  $R_{1.4} = 11.8^{+1.2}_{-0.7} \text{ km}$  and  $BE_{1.4} = 0.16^{+0.01}_{-0.02} M_\odot$  if the constraints from the nuclear data and the gravitational-wave data have been jointly applied. For the joint analysis of gravitational-wave data and the LMXB data, we have  $I_{1.4} = 1.28^{+0.15}_{-0.08} \times 10^{38} \text{ kg} \cdot \text{m}^2$ ,  $\Lambda_{1.4} = 220^{+90}_{-90}$ ,  $R_{1.4} = 11.1^{+0.7}_{-0.6} \text{ km}$ , and  $BE_{1.4} = 0.18^{+0.01}_{-0.01} M_\odot$ . These results suggest that the current constraints on  $\Lambda$  and  $R$  still suffer from significant systematic uncertainties, while  $I_{1.4}$  and  $BE_{1.4}$  are better constrained.

## 1. INTRODUCTION

As the compact objects contain material with the highest densities in the observable universe, neutron stars (NSs) serve as the ideal laboratories for studying extremely dense matter (see, e.g. Lattimer 2012; Lattimer & Prakash 2016; Özel & Freire 2016; Oertel et al. 2017, for recent reviews). So far, about 2000 NSs, mainly consisting of pulsars<sup>1</sup>, have been measured in the Galaxy. The measurements of masses and/or radii for a small fraction of NSs have set interesting constraints on the properties of the very dense matter. For example, the detections of a few NSs with a gravitational mass of  $\approx 2M_\odot$  (Demorest et al. 2010; Antoniadis et al. 2013; Cromartie et al. 2019) have excluded the soft equations of states (EoSs) that are unable to support such massive objects. For some NSs in the LMXB systems, there is a good opportunity to measure their radius and mass simultaneously via spectroscopic observation of the thermonuclear burst that happened on their surfaces,

or through observations of their angular size when they remain in the quiescent state (see, e.g. Özel & Freire 2016, for a comprehensive review). These radii/masses data have been widely adopted to constrain the EoS of ultra-high-dense matter (Özel & Psaltis 2009; Steiner et al. 2010, 2013; Lattimer & Steiner 2014a,b; Nättilä et al. 2016; Özel et al. 2016; Raithel et al. 2017; Baillot d’Etivaux et al. 2019; Fasano et al. 2019).

Nuclear experiments are also progressively narrowing down the ranges of parameters that describe the symmetry energy near the nuclear saturation density, which can be further adopted to infer the physical properties of NSs (Lattimer & Lim 2013; Lim & Holt 2018; Krastev, & Li 2019) including, for instance, the radii, moments of inertia, and the binding energy.

The discovery of the first NS merger-driven gravitational-wave event GW170817 (Abbott et al. 2017a) has provided the community with a valuable/novel opportunity to reliably probe the EoS and the NS properties. In particular, with some reasonable assumptions and EoS-independent relationships, the tidal deformabilities and the radii of the two NSs involved in GW170817 have been measured and some bulk properties of NSs have

tangsp@pmo.ac.cn (SPT) and yzfan@pmo.ac.cn (YZF)

<sup>1</sup> <http://www.atnf.csiro.au/research/pulsar/psrcat>

been inferred (e.g., Annala et al. 2018; Fattoyev et al. 2018; Most et al. 2018; Lim & Holt 2018; De et al. 2018; Abbott et al. 2018; Landry & Kumar 2018; Lim & Holt 2019; Kumar, & Landry 2019).

Inspired by the above remarkable advances, in this work we try to further explore the potential of constraining the EoS of dense NS matter with the mass ( $M$ ) and/or radius ( $R$ ) measurements of the NSs, the nuclear experimental data, and GW170817. Special attention is paid to the dependence of the results on the data set adopted in the investigation.

This work is organized as follows. In Section 2 we introduce the methods. The results on the EoS constraints and bulk properties of NSs are presented in Section 3. Section 4 is our summary and discussion.

## 2. METHODS

### 2.1. Parameterizing EoS

Parameterized representations of the EoS play a very important role in efforts to measure the properties of the matter in the cores of NSs using astronomical observations and the gravitational-wave data. A number of methods to effectively parameterize the realistic EOS models have been developed in the literature (Lindblom 2010; Kurkela et al. 2014; Steiner et al. 2016; Lim & Holt 2019; McNeil Forbes et al. 2019), including, for instance, the spectral expansion (Lindblom 2010) and the piecewise polytropic expansion (Read et al. 2009a; Özel & Freire 2016; Raithel et al. 2017).

Usually, the piecewise polytropic expansion can be carried out in four ways. The first approach is to introduce a set of pressures at given densities to approximate the EoS (Özel & Freire 2016; Raithel et al. 2017). The second is to adopt a series of adiabatic indexes in given density ranges (Read et al. 2009a). The third is to parameterize pressure difference between two neighboring fixed densities (Steiner et al. 2016). The last is to parameterize densities and pressures simultaneously (Steiner et al. 2016). In each case, the EoS in each density range can be expressed as

$$P = K\rho^\Gamma, \quad (1)$$

where  $P$  is the pressure,  $\rho$  is the mass density,  $K$  is constant in each piece of EoS, and  $\Gamma$  is the adiabatic index. Here, we adopt the first method by parameterizing EoS using four pressures  $\{P_1, P_2, P_3, P_4\}$  at the corresponding densities of  $\{1, 1.85, 3.7, 7.4\}\rho_{\text{sat}}$  (Özel & Psaltis 2009), where  $\rho_{\text{sat}} = 2.7 \times 10^{14} \text{g/cm}^3$  is the so-called saturation density.

With a specific parameterized EoS in hand, we need one additional parameter, the central pseudo-enthalpy ( $h_c$ ), to determine the global properties of non-rotating

NSs such as the gravitational mass  $M$ , the mean radius  $R$  and the dimensionless tidal deformability  $\Lambda$ , etc. The  $h_c$  is defined as

$$h_c \equiv \int_0^{p_c} \frac{dp}{\epsilon(p) + p}, \quad (2)$$

where  $p$  is the pressure,  $\epsilon$  is the energy density, and  $p_c$  is the pressure at the center of the NS.

We implement method described in Appendix C of Lindblom & Indik (2014) to calculate the global properties  $\{M, R, \Lambda\}$  from parameters  $\{h_c, P_1, P_2, P_3, P_4\}$ . A common EoS table for  $\rho \leq 0.33\rho_{\text{sat}}$  is adopted from SLy EoS table (Özel et al. 2016)<sup>2</sup>.

For convenience, hereafter we replace the EoS parameters  $\{P_1, P_2, P_3, P_4\}$  with the equivalent dimensionless parameters  $\{\hat{p}_1, \hat{p}_2, \hat{p}_3, \hat{p}_4\}$ , where  $\hat{p}_i = P_i/(10^{32+i} \text{dyn cm}^{-2})$ .

### 2.2. Priors and known constraints of the EoS parameters

We use a flat prior for every pressure parameters unless with a specific statement. The ranges of these parameters are set to be consistent with realistic EoSs of dense matter shown in Read et al. (2009a)<sup>3</sup>, namely  $\hat{p}_1 \in [1.5, 13.5]$ ,  $\hat{p}_2 \in [0.7, 8.0]$ ,  $\hat{p}_3 \in [0.6, 7.0]$ , and  $\hat{p}_4 \in [0.3, 4.0]$ . In additionally, the EoS parameters  $\{P_1, P_2, P_3, P_4\}$  should satisfy the following constraints (Raithel et al. 2017):

- (i) The microscopical stability, i.e.,  $P_4 \geq P_3 \geq P_2 \geq P_1$ .
- (ii) The physically plausible condition of causality, i.e.,

$$\frac{c_s^2}{c^2} = \frac{dp(h)}{d\epsilon(h)} \leq 1 \quad \text{for } h \leq h_{c,\text{max}}, \quad (3)$$

where  $p(h)$ ,  $\epsilon(h)$ ,  $h$ , and  $c$  are pressure, energy density, pseudo-enthalpy, speed of the light, respectively.  $h_{c,\text{max}}$  is the central enthalpy of a non-rotating stable NS with a maximal gravitational mass ( $M_{\text{TOV}}$ ).

(iii) Maximum stable mass of non-rotating NS ( $M_{\text{TOV}}$ ) is likely within the range of  $[2.06, 2.5]M_\odot$  (Akmal et al. 1998; Lattimer & Prakash 2016)<sup>4</sup>. The lower

<sup>2</sup> <http://xtreme.as.arizona.edu/NeutronStars>

<sup>3</sup> The exception is that for Test F we have to take significantly wider prior distributions of the pressure parameters, otherwise it is not possible to well reproduce the  $M$ - $R$  distributions reported in Özel et al. (2016), as very small radii were suggested for a few sources. Most of the “enlarged” regions, however, are found to be rejected by physical conditions such as causality and  $M_{\text{TOV}}$  limit.

<sup>4</sup> In the literature, some tighter bounds on  $M_{\text{TOV}}$  have been suggested (e.g., Fan et al. 2013). However, these bounds are highly model-dependent and in the current analysis we do not take them into account.

limit is taken to be slightly smaller than the 68.3% lower limit of the mass of PSR J0740+6620 (Cromarite et al. 2019), i.e.,  $2.07M_\odot$ . This is because PSR J0740+6620 has a rotation frequency of 346.532 Hz, which can slightly weaken the constraints on the  $M_{\text{TOV}}$  to a value of  $2.06M_\odot$  (see Breu & Rezzolla 2016; Ma et al. 2018, for some relevant discussions).

(iv) The adiabatic indexes in all the plausible density regions should satisfy the condition  $\Gamma < 7$  (Fasano et al. 2019).

### 2.3. LMXB data

As mentioned in Section 2.1, given a set of parameters  $\{h_c, \hat{p}_1, \hat{p}_2, \hat{p}_3, \hat{p}_4\}$ , one can derive the mass and the radius of an NS. While the observations of an LMXB system yield the probability distribution function of the masses and the radii of the NSs. Thus, if we take these sources into consideration, the likelihood for these galactic NSs then takes the form

$$L_{GN}(\vec{\theta}_{GN}) = \prod_{i=1}^n P_i(M(\vec{\theta}_i), R(\vec{\theta}_i)), \quad (4)$$

where  $n$  is the number of NSs taken in this analysis,  $P_i$  is the likelihood at  $\{M(\vec{\theta}_i), R(\vec{\theta}_i)\}$  interpolated from the likelihood table of the  $i$ th source Özel et al. (2016), and  $\vec{\theta}_i := \{h_{ci}, \hat{p}_1, \hat{p}_2, \hat{p}_3, \hat{p}_4\}$  are the basic parameters to describe a cold non-rotating NS. Thus, the  $\vec{\theta}_{GN}$  can take the form

$$\vec{\theta}_{GN} := \cup_{i=1}^n \vec{\theta}_i = \{h_{ci} | i = 1, 2, 3, \dots, n\} \\ \cup \{\hat{p}_1, \hat{p}_2, \hat{p}_3, \hat{p}_4\},$$

which contains two parts, i.e., four EoS parameters and the central enthalpies of  $n$  NSs.

Six sources, namely 4U 1820-30, 4U 1724-207, EXO 1745-248, SAX J1748.9-2021, KS1731-260 and 4U 1608-52, whose masses and radii are constrained by thermonuclear burst data, have been taken into account in our analysis. The masses, radii, and associated likelihood data are directly taken from Özel et al. (2016, see the web source (see footnote 2)). The pseudo-enthalpy at the center of each galactic NS  $h_{ci}$  is assumed to span uniformly in the range  $[0.1, 0.8]$ .

### 2.4. Symmetry energy

We know that nuclear experiments can also contribute to constraining the EoS parameters (e.g. Lattimer & Lim 2013). In  $\beta$ -equilibrium condition, the pressure of matter at neutron saturation density satisfies (Lattimer & Steiner 2014a)

$$p_\beta(n_s) \simeq \frac{L}{3} n_s \left[ 1 - \left( \frac{4S_v}{\hbar c} \right)^3 \frac{4 - 3S_v/L}{3\pi^2 n_s} + \dots \right] \quad (5)$$

where  $n_s = 0.16 \text{ fm}^{-3}$  is the saturation baryon number density,  $(S_v, L)$  are symmetry parameters, and  $\hbar$  is the reduced Planck constant. We take the bounds on  $S_v, L$  found in Tews et al. (2017), and apply a similar process used in Lattimer & Steiner (2014a) to transform these constraints to a distribution of  $p_\beta(n_s)$  using equation (5) with Monte Carlo sampling. Then, we can obtain a 95% confidence interval of pressure  $\hat{p}_1$  at  $n_s$ , which is  $[3.12, 4.70]$ . Meanwhile, Özel et al. (2016) also found a constraint  $P_2 > 7.56 \text{ MeV fm}^{-3}$  using nuclear data, which corresponds to our parameter  $\hat{p}_2 > 1.21$ . If we take these nuclear constraints into analysis, the likelihood for these constraints should read

$$L_{Nuc}(\vec{\theta}_{Nuc}) = \begin{cases} 1 & (3.12 < \hat{p}_1 < 4.70, \hat{p}_2 > 1.21) \\ -\infty & (\text{Otherwise}) \end{cases}, \quad (6)$$

where  $\vec{\theta}_{Nuc} := \{\hat{p}_1, \hat{p}_2, \hat{p}_3, \hat{p}_4\}$ .

### 2.5. GW data

Instead of sampling the parameters  $\{M_1, M_2, \Lambda_1, \Lambda_2\}$  in usual analyses of GW170817 data, we sample  $\{\mathcal{M}_c, q, \hat{p}_1, \hat{p}_2, \hat{p}_3, \hat{p}_4\}$  to determine the former four parameters.  $M_1$  and  $M_2$  are determined by equations

$$M_1 = q^{2/5}(q+1)^{1/5} \mathcal{M}_c, \quad (7) \\ M_2 = q^{-3/5}(q+1)^{1/5} \mathcal{M}_c,$$

where  $\mathcal{M}_c$  is chirp mass and  $q$  is mass ratio. Note that here  $M_1$  and  $M_2$  are detector frame parameters, but we can just calculate the source frame masses through parameterized EoSs, so we optimize central enthalpy  $h_{c1}$  and  $h_{c2}$  to get  $M_1/(1+z)$  and  $M_2/(1+z)$ , respectively, where  $z = 0.0099$  is the geocentric redshift of the source of GW170817 (Levan et al. 2017; Abbott et al. 2019) inferred from the electromagnetic observations of the host galaxy NGC4993. Then we can combine four pressure parameters and optimized central enthalpy  $h_{c1}^{\text{opt}}(h_{c2}^{\text{opt}})$  to calculate  $\Lambda_1(\Lambda_2)$ .

We restrict the sky location to the known position of SSS17a/AT 2017gfo (Abbott et al. 2017b) following Abbott et al. (2019), and assume the spin of each NS is aligned with the orbital angular momentum. Additionally, we marginalize phase and distance over likelihood, because they have little correlation with parameters we care about (Allen et al. 2012; Abbott et al. 2019; Radice & Dai 2019), and by this mean we can save much time in Markov chain Monte Carlo (MCMC) sampling.

Based on the above considerations, if we take the GW170817 into analysis, the likelihood for the gravitational-wave (Allen et al. 2012) of each detector

would have the functional form

$$L_{GW}(\vec{\theta}_{GW}) \propto \exp \left[ -2 \int_0^\infty \frac{|\tilde{d}(f) - \tilde{h}(f; \vec{\theta}_{GW})|^2}{S_n(f)} df \right], \quad (8)$$

where

$$\vec{\theta}_{GW} := \{\hat{p}_1, \hat{p}_2, \hat{p}_3, \hat{p}_4\} \cup \{\mathcal{M}_c, q, \chi_1, \chi_2, \theta_{jn}, t_c, \Psi\},$$

$\chi_i (i = 1, 2)$ ,  $\theta_{jn}$ ,  $t_c$  and  $\Psi$  are spin magnitudes of NS, the angle between the line of sight and the binary NS system's total angular momentum, the GPS time when the coalescence signal reaches the geocenter of the Earth, and polarization, respectively.  $\tilde{d}(f)$ ,  $S_n(f)$ , and  $\tilde{h}(f; \vec{\theta}_{GW})$  are the Fourier transform of the time domain signal of GW170817, the power spectral density of the data, and the frequency domain strain data generated using the parameter  $\vec{\theta}_{GW}$ , respectively. And we evaluate this part of the likelihood using PyCBC Inference package (The PyCBC Team 2018; Biwer et al. 2019).

We take publicly available cleaned 4096 Hz gravitational-wave data<sup>5</sup> lying in the GPS time segment [1, 187, 008, 682, 1, 187, 008, 890]s into analysis. An aligned spin prior and a cosine uniform prior of orbital inclination angle  $\theta_{jn}$  are adopted. Moreover,  $\mathcal{M}_c$ ,  $q$  (the mass ratio),  $\chi_i (i = 1, 2)$ ,  $\Psi$  and  $t_c$  distribute uniformly in the range [1.18, 1.21] $M_\odot$ , [0.5, 1.0], [0, 0.05], [0, 2 $\pi$ ] and [1, 187, 008, 882, 1, 187, 008, 883] s, respectively.

### 2.6. Joint analysis

To sample a group of parameters in the MCMC procedure, we need a likelihood describing how probable the data could be given a specific group of parameters and a prior probability of these parameters. Below we examine the roles of different sets of data and/or constraints/assumptions in reconstructing the EoS (see Table 1) by setting different likelihoods/priors in each analysis as follows:

(A) The gravitational-wave data of GW170817 and the default constraints on  $M_{TOV}$  (i.e.,  $\in [2.06, 2.5]M_\odot$ ). The priors of four pressure parameters have been introduced in Section 2.2. The waveform model PhenomD-NRT is adopted. The total likelihood is  $L_{GW}(\vec{\theta}_{GW})$  and the number of free parameters is 11.

(B) The same as scenario (A) except a more ‘‘conservative’’ bound on  $M_{TOV}$  (i.e.,  $M_{TOV} \in [1.97, 2.8]M_\odot$ ) is considered.

(C) The same as scenario (A) except that the waveform model TaylorF2 is used.

(D) The same as scenario (A) except that the log-uniform prior for every pressure parameters has been assumed.

(E) In comparison to scenario (A), additional constraints from the symmetry energies have been imposed (see Section 2.4). The total likelihood is given by

$$L(\vec{\theta}) = L_{GN}(\vec{\theta}_{GW}) \times L_{Nuc}(\vec{\theta}_{Nuc}), \quad (9)$$

where

$$\vec{\theta} = \vec{\theta}_{GW} \cup \vec{\theta}_{Nuc} = \{\hat{p}_1, \hat{p}_2, \hat{p}_3, \hat{p}_4\} \cup \{\mathcal{M}_c, q, \chi_1, \chi_2, \theta_{jn}, t_c, \Psi\},$$

and there are 11 parameters total.

(F) The same as scenario (A) except for the inclusion of six LMXB sources with thermonuclear bursts. The total likelihood is given by

$$L(\vec{\theta}) = L_{GN}(\vec{\theta}_{GN}) \times L_{GW}(\vec{\theta}_{GW}), \quad (10)$$

where

$$\vec{\theta} = \vec{\theta}_{GN} \cup \vec{\theta}_{GW} = \{h_{ci} | i = 1, 2, 3, \dots, n\} \cup \{\hat{p}_1, \hat{p}_2, \hat{p}_3, \hat{p}_4\} \cup \{\mathcal{M}_c, q, \chi_1, \chi_2, \theta_{jn}, t_c, \Psi\}.$$

There are 17 free parameters in total, as we adopt six LMXB sources ( $n = 6$ ) in the analysis.

Our MCMC sampling is carried out using the Bilby (Ashton et al. 2019) built-in sampler PyMultiNest (Buchner 2016).

## 3. RESULTS

We calculate Kullback-Leibler divergence (KLD) between prior and posterior following Abbott et al. (2019) to evaluate how much parameter information is extracted from the data. The KLD between distribution  $p$  and  $q$  reads

$$D_{KL}(p|q) = \int p(x) \log_2 \left( \frac{p(x)}{q(x)} \right) dx, \quad (11)$$

where  $x$  runs over the whole possible range of a parameter. A higher  $D_{KL}$  means more parameter information can be extracted from data. In other words, the parameter is well constrained in comparison to the prior.

We can also reconstruct  $\tilde{\Lambda}$  using samples of  $\{\mathcal{M}_c, q, \hat{p}_1, \hat{p}_2, \hat{p}_3, \hat{p}_4\}$  in each Test. This is done by determining  $\{M_1, M_2, \Lambda_1, \Lambda_2\}$  from  $\{\mathcal{M}_c, q, \hat{p}_1, \hat{p}_2, \hat{p}_3, \hat{p}_4\}$  as described in Section 2.5, and then calculate

$$\tilde{\Lambda} := \frac{16}{13} \left[ \frac{(M_1 + 12M_2)M_1^4\Lambda_1}{(M_1 + M_2)^5} + (1 \leftrightarrow 2) \right]$$

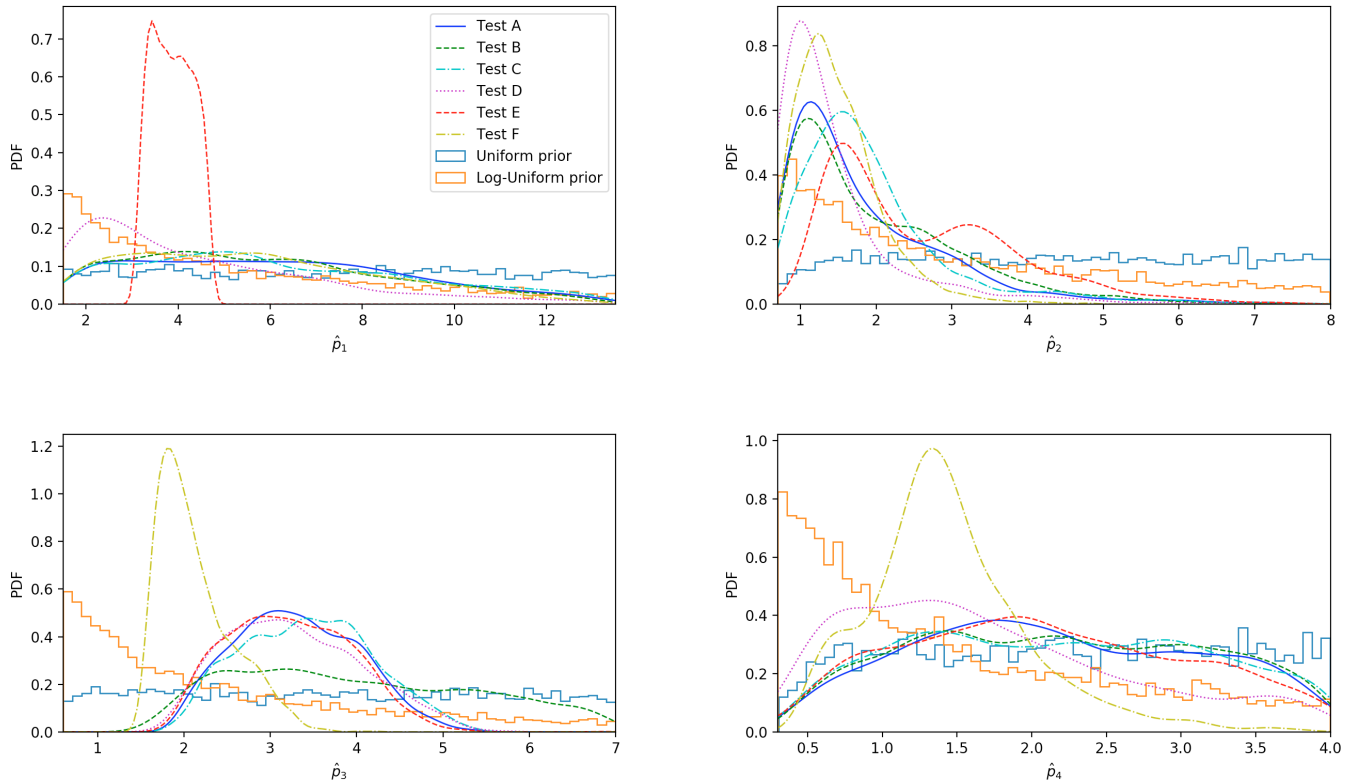
. Similarly, using the posterior samples of EoS parameters  $\{\hat{p}_1, \hat{p}_2, \hat{p}_3, \hat{p}_4\}$ , we can optimize  $h_c$  for each single posterior sample to get NS with mass  $1.4M_\odot$  and then calculate its bulk properties, such as  $R_{1.4}$  and  $\Lambda_{1.4}$ . To avoid the possible bias of bulk properties caused by the

<sup>5</sup> <https://www.gw-openscience.org>

**Table 1.** Different Tests Designed to Show How Different Assumptions can Affect the EoS Constraint

Condition / Test	Test A	Test B	Test C	Test D	Test E	Test F
LMXB data considered	No	No	No	No	No	Yes
GW data considered	Yes	Yes	Yes	Yes	Yes	Yes
Nuclear constraints	No	No	No	No	Yes	No
Waveform model	IMRPNRT <sup>a</sup>	IMRPNRT	TaylorF2	IMRPNRT	IMRPNRT	IMRPNRT
$M_{\text{TOV}}/M_{\odot}$ range	[2.06, 2.5]	[1.97, 2.8]	[2.06, 2.5]	[2.06, 2.5]	[2.06, 2.5]	[2.06, 2.5]
Prior of pressures	Uniform	Uniform	Uniform	Log Uniform	Uniform	Uniform

<sup>a</sup>Short note of PhenomDNRT waveform model

**Figure 1.** Posterior distributions of four pressure parameters in different tests.**Table 2.** KL-divergence (in bits) Between the Prior and Posterior Distribution for Pressure Parameters in Different Tests

Test / $D_{KL}$	$D_{KL}^{\hat{p}_1}$	$D_{KL}^{\hat{p}_2}$	$D_{KL}^{\hat{p}_3}$	$D_{KL}^{\hat{p}_4}$
Test A	$0.22^{+0.05}_{-0.04}$	$1.85^{+0.21}_{-0.22}$	$0.66^{+0.11}_{-0.09}$	$0.11^{+0.03}_{-0.03}$
Test B	$0.31^{+0.03}_{-0.02}$	$1.79^{+0.13}_{-0.16}$	$0.17^{+0.02}_{-0.02}$	$0.09^{+0.02}_{-0.01}$
Test C	$0.21^{+0.02}_{-0.02}$	$1.79^{+0.09}_{-0.09}$	$0.55^{+0.05}_{-0.05}$	$0.11^{+0.02}_{-0.02}$
Test D	$0.18^{+0.05}_{-0.04}$	$0.91^{+0.12}_{-0.10}$	$1.12^{+0.22}_{-0.56}$	$0.42^{+0.08}_{-0.07}$
Test E	$0.51^{+0.14}_{-0.13}$	$1.35^{+0.15}_{-0.19}$	$1.09^{+0.16}_{-0.26}$	$0.17^{+0.04}_{-0.04}$
Test F	$0.45^{+0.07}_{-0.07}$	$2.12^{+0.28}_{-0.28}$	$1.73^{+0.24}_{-0.35}$	$1.30^{+0.15}_{-0.17}$

Note. The median and 90% interval are evaluated by repeatedly draw samples from posterior and prior, with each draw gives a KLD value.

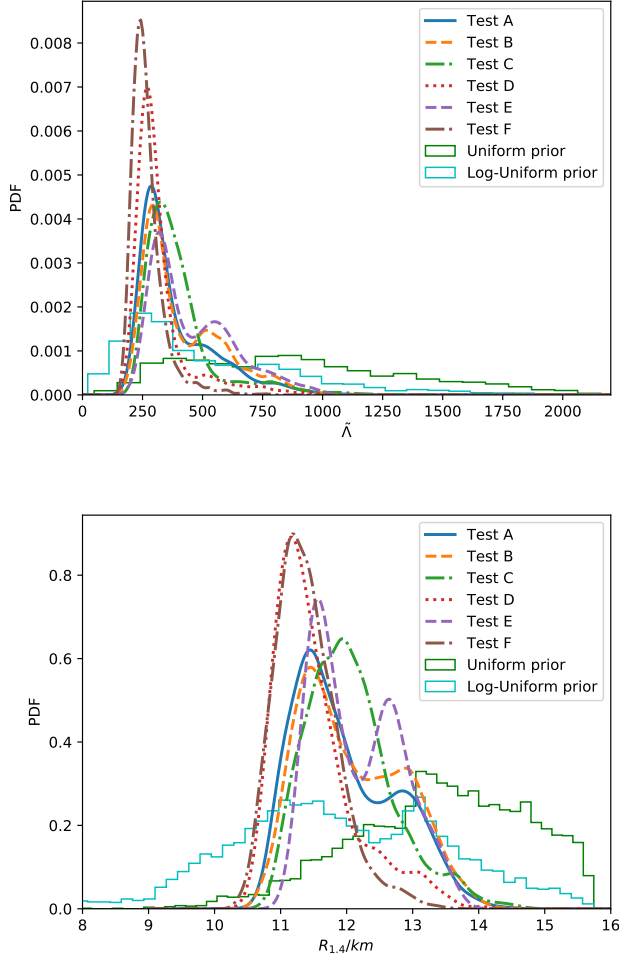
prior of the pressure parameters (from the solid green and cyan line in Figure 2, we can see that this effect is worth noticing), we use the method described in Abbott et al. (2019) to divide the Kernel Density Estimation (KDE) of the posterior by that of the prior (i.e. to reweight the posterior with prior) and then calculate the 90% highest posterior density (HPD) intervals of bulk properties (see Table 4).

### 3.1. Constraining the EoS

The gravitational-wave data alone can only constrain  $\hat{p}_2$  relatively well (see Test B in Figure 1 and Table 2), likely because the information of tidal deformability en-

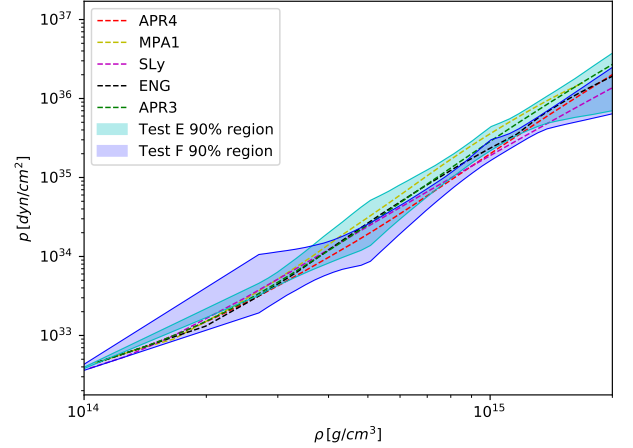
**Table 3.** 68% and 95% Ranges of Four Pressure Parameters in Different Tests

Test / Parameter	$\hat{p}_1$		$\hat{p}_2$		$\hat{p}_3$		$\hat{p}_4$	
	68%	95%	68%	95%	68%	95%	68%	95%
Test A	$5.9^{+3.4}_{-3.0}$	$5.9^{+6.5}_{-4.2}$	$1.5^{+1.4}_{-0.5}$	$1.5^{+3.3}_{-0.7}$	$3.3^{+0.8}_{-0.7}$	$3.3^{+1.4}_{-1.2}$	$2.1^{+1.2}_{-0.9}$	$2.1^{+1.8}_{-1.5}$
Test B	$5.5^{+3.5}_{-2.6}$	$5.5^{+6.5}_{-3.8}$	$1.7^{+1.5}_{-0.7}$	$1.7^{+3.3}_{-0.9}$	$3.8^{+1.8}_{-1.3}$	$3.8^{+2.9}_{-2.0}$	$2.2^{+1.1}_{-1.0}$	$2.2^{+1.7}_{-1.6}$
Test C	$5.6^{+3.9}_{-2.7}$	$5.6^{+6.9}_{-3.9}$	$1.7^{+0.9}_{-0.6}$	$1.7^{+3.2}_{-0.9}$	$3.4^{+0.8}_{-0.8}$	$3.4^{+1.5}_{-1.3}$	$2.2^{+1.1}_{-1.1}$	$2.2^{+1.7}_{-1.6}$
Test D	$3.6^{+3.3}_{-1.6}$	$3.6^{+7.4}_{-2.1}$	$1.2^{+0.8}_{-0.3}$	$1.2^{+3.1}_{-0.5}$	$3.2^{+0.9}_{-0.7}$	$3.2^{+1.7}_{-1.2}$	$1.5^{+1.2}_{-0.8}$	$1.5^{+2.2}_{-1.0}$
Test E	$3.9^{+0.5}_{-0.5}$	$3.9^{+0.8}_{-0.7}$	$2.2^{+1.6}_{-0.8}$	$2.2^{+3.4}_{-1.0}$	$3.2^{+0.8}_{-0.7}$	$3.2^{+1.4}_{-1.1}$	$2.0^{+1.2}_{-0.9}$	$2.0^{+1.9}_{-1.4}$
Test F	$5.4^{+3.3}_{-2.6}$	$5.4^{+6.1}_{-3.7}$	$1.4^{+0.6}_{-0.4}$	$1.4^{+1.5}_{-0.7}$	$2.0^{+0.6}_{-0.3}$	$2.0^{+1.1}_{-0.4}$	$1.4^{+0.5}_{-0.4}$	$1.4^{+1.4}_{-0.8}$

**Figure 2.** The upper panel shows the dimensionless tidal deformability reconstructed from posterior samples. The lower panel presents the  $R_{1.4}$  inferred from each posterior sample.

coded in the late inspiral state is mostly carried by this parameter (Read et al. 2009b).

The relative tight constraints on  $M_{\text{TOV}}$  help to narrow down the posterior range of  $\hat{p}_3$ , but have little influence on  $\hat{p}_1$ ,  $\hat{p}_2$ , and  $\hat{p}_4$  (see Figure 1). This is also evident in Table 2. The KLDs of  $\hat{p}_1$ ,  $\hat{p}_2$  and  $\hat{p}_4$  in Test A and Test B

**Figure 3.** The 90% confidence region of the EoS and some realistic EoSs.

are almost the same, while the KLD of  $\hat{p}_3$  changes significantly. This fact indicates that  $M_{\text{TOV}}$  may be mainly governed by  $\hat{p}_3$  rather than other parameters (Özel & Psaltis 2009; Read et al. 2009a).

We can see from Figure 2 that a tighter mass constraint causes a slight decrease of  $\tilde{\Lambda}$  and  $R_{1.4}$ . Differing from this work, Abbott et al. (2018) found a strong influence of  $M_{\text{TOV}}$  on the radius of the NS. Note that Abbott et al. (2018) adopted a spectral expansion method to parameterize the EoS, while we take a piecewise expansion. The difference in the results may be attributed to the different ways of parameterizing the EoS, as also found in the literature (e.g. Nättilä et al. 2016; Fasoano et al. 2019). The reason comes partly from the fact that different parameterization methods already give different priors to the global properties of the EoS (Steiner et al. 2013), thus a prior-reweighted posterior of global properties of EoS is needed (see Table 4).

The results can also be dependent of the waveform model. In comparison to the Test A, the adoption of a different waveform model TaylorF2 (i.e., the Test C) in the analysis leads to a slight decrease of coalescence time

(see Figure 5 in the Appendix A), and a small increase of  $\hat{p}_2$  (see Figure 1),  $\tilde{\Lambda}$ ,  $\Lambda_{1.4}$ , and  $R_{1.4}$  (see Figure 2 and Table 4). But no shifts have been observed if the SEOBNRT waveform model is adopted instead.

Changing a flat prior to a log-uniform prior (i.e., Test D) slightly modifies the posterior shapes of  $\hat{p}_2$  and  $\hat{p}_3$ , while the posterior shapes of  $\hat{p}_1$  and  $\hat{p}_4$  simply follow the prior shapes. This suggests that  $\hat{p}_2$  and  $\hat{p}_3$  are relatively well constrained by the gravitational-wave data and the maximum mass constraint, but  $\hat{p}_1$  and  $\hat{p}_4$  are not (see also Table 2). Also, changing a flat prior to a log-uniform prior leads to a decrease in the posterior of  $\tilde{\Lambda}$  and  $R_{1.4}$  (see Figure 2), but we note that after reweighting the posterior with the prior, the HPD range of  $\tilde{\Lambda}$  and  $R_{1.4}$  in Test A are consistent with those in Test D (see Table 4). The consistency after re-weighting the posterior with the prior in different analyses that use different priors also provides a proof of the robustness of our results and the importance of reweighting a posterior with a prior.

The addition nuclear constraints (i.e., Test E) sharply narrows down the prior range of  $\hat{p}_1$ , and boosts  $\hat{p}_2$  to a slightly higher value, but does not help constraining  $\hat{p}_3$  and  $\hat{p}_4$  (see Figure 1 and Table 3). Additionally, the inclusion of the nuclear constraints favors larger  $\tilde{\Lambda}$ ,  $R_{1.4}$ , and  $\Lambda_{1.4}$  than Test A (see Figure 2 and Table 4).

The joint constraints on the EoS by the LMXB sources with thermonuclear bursts and gravitational-wave data (i.e., Test F) can well constrain  $\hat{p}_2$ ,  $\hat{p}_3$ , and  $\hat{p}_4$  (see Figure 1 and Table 2). The constraint on  $\hat{p}_2$  mainly comes from radius measurement of these sources, because the radius of an NS is mainly determined by  $\hat{p}_2$  (Lattimer & Prakash 2001). Our  $R_{1.4}$  (see Table 4) is larger than that of Guillot et al. (2013); the difference may come from the fact that they use the quiescent LMXB data, but we use the data of LMXB sources with thermonuclear bursts.

In particular, small  $R_{1.4}$  and  $\Lambda_{1.4}$  are produced (see also Fasano et al. 2019) in Test F, differing from what we have found in Test E, and indicating that the nuclear data and the  $M/R$  measurement of LMXB sources that have thermonuclear bursts may not be fully consistent with each other. Such a tension may be resolved in the future as long as the nuclear data can be better measured/understood and the measurements of the NSs in the LMXB sources with thermonuclear bursts have been significantly improved (so far, the measured radii can still suffer from serious systematic uncertainties).

Our gravitational-wave parameters are nicely in agreement with Abbott et al. (2019) in all six tests (see the Appendix A). Additionally, as shown in Figure 2 and Table 4, for both Test A and Test C, the resulting  $\tilde{\Lambda}$  are also consistent with Abbott et al. (2019).

**Table 4.** 90% HPD Range of a Prior-reweighted Posterior of  $R_{1.4}$ ,  $\Lambda_{1.4}$  and  $\tilde{\Lambda}$  Directly Inferred from Posterior Samples of  $\{\hat{p}_1, \hat{p}_2, \hat{p}_3, \hat{p}_4\}$

Test/Property	$R_{1.4}/km$	$\Lambda_{1.4}$	$\tilde{\Lambda}$
Test A	$11.5^{+1.5}_{-0.8}$	$300^{+300}_{-130}$	$310^{+320}_{-160}$
Test B	$11.5^{+1.5}_{-0.9}$	$330^{+310}_{-170}$	$340^{+350}_{-190}$
Test C	$11.7^{+1.0}_{-0.9}$	$320^{+280}_{-160}$	$350^{+270}_{-200}$
Test D	$11.4^{+1.3}_{-0.8}$	$290^{+310}_{-140}$	$310^{+340}_{-180}$
Test E	$11.8^{+1.2}_{-0.7}$	$390^{+280}_{-210}$	$400^{+310}_{-230}$
Test F	$11.1^{+0.7}_{-0.6}$	$220^{+90}_{-90}$	$260^{+90}_{-190}$

**Table 5.** 90% Interval of Dimensionless Tidal Deformability, Moment of Inertia and Binding Energy of an NS with Gravitational Mass  $1.4M_{\odot}$

Samples	$\Lambda_{1.4}$	$I_{1.4}/10^{38} \text{kg} \cdot \text{m}^2$	$BE_{1.4}/M_{\odot}$
Sample A	$360^{+370}_{-110}$	$1.43^{+0.30}_{-0.13}$	$0.16^{+0.01}_{-0.02}$
Sample B	$230^{+130}_{-50}$	$1.28^{+0.15}_{-0.08}$	$0.18^{+0.01}_{-0.01}$
Sample C	$190^{+390}_{-120}$	$1.23^{+0.41}_{-0.24}$	$0.18^{+0.03}_{-0.03}$
Sample D	$350^{+370}_{-190}$	$1.42^{+0.30}_{-0.25}$	$0.16^{+0.02}_{-0.02}$

Note. These properties are inferred from posterior samples of  $\{M_1, M_2, \Lambda_1, \Lambda_2\}$  and universal relations described in the main text.

With the posterior of pressure parameters, it is straightforward to calculate the allowed region of the EoS. As shown in Figure 3, in comparison to the default scenario (Test A), Test F can improve the constraints in the high-density region while Test E can better constrain the low-density region. We also compare these results with some realistic EoSs (see the web reference in footnote 2) and find reasonable agreement. Since the start of the O3 run of advanced LIGO/Virgo in 2019 April, a few NS merger gravitational-wave events have been reported<sup>6</sup>. The release of these new data is expected to significantly improve the constraints on the EoS of NSs.

### 3.2. Constraining the properties of galactic double NS systems

With the posterior samples of  $\{M_1, M_2, \Lambda_1, \Lambda_2\}$  of GW170817 and some “universal” relations, it is possible to “extrapolate” these properties to similar masses and thus get the constraints of some global properties at these given masses, in particular those accurately measured for the galactic double NS systems (Landry & Kumar 2018; Kumar, & Landry 2019).

#### 3.2.1. Constraint method

<sup>6</sup> <https://gracedb.ligo.org/latest/>

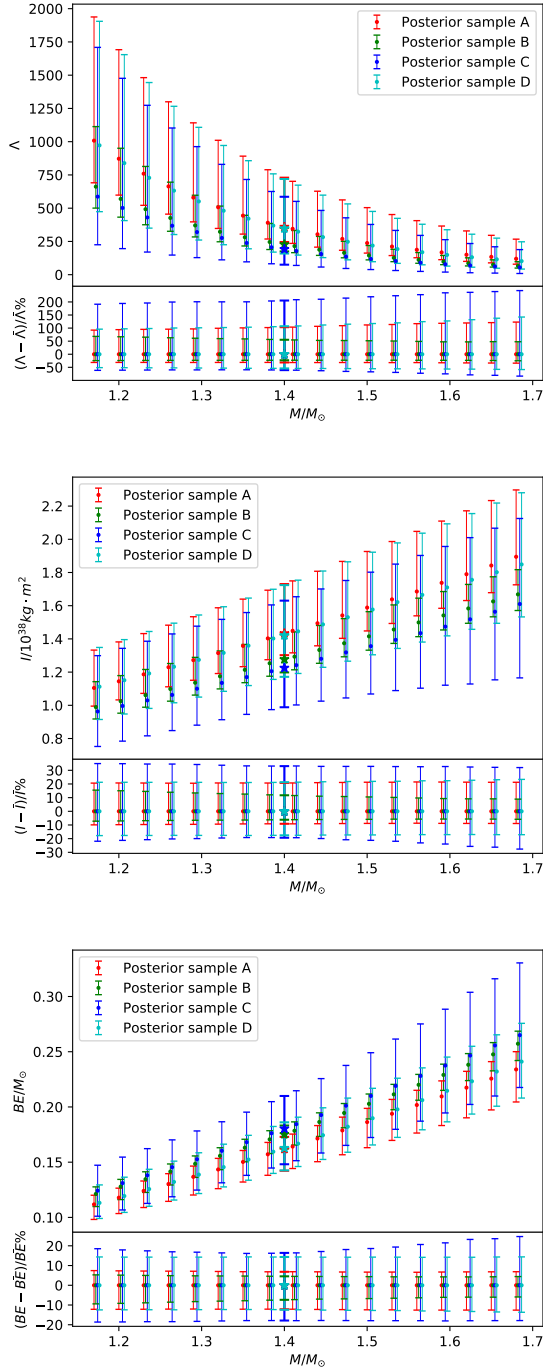


**Figure 4.** Upper panel: 90% interval of dimensionless tidal deformability and its relative error. Middle panel: 90% interval of moment of inertia and its relative error. Lower panel: 90% interval of binding energy and its relative error. These intervals are all calculated from different groups of posterior samples and universal relations at each mass. Here the red, green, blue, and cyan error bars respectively show the 90% intervals for Posterior Samples A, B, C and D. The stars show the constraint at the canonical mass  $M = 1.4M_{\odot}$ .

Tidal deformability can be expanded into a Taylor series around a “canonical” reference mass  $M_{\text{ref}}$  (Del Pozzo et al. 2013). Below we adopt a linear expansion following Del Pozzo et al. (2013) and Abbott et al. (2018)

$$\lambda(M) \simeq \lambda_{\text{ref}} + \lambda^1(M - M_{\text{ref}})/M_{\odot}, \quad (12)$$

where  $\lambda(M) \equiv \Lambda(M)(GM/c^2)^5$  is the tidal deformability of the NS with a gravitational mass  $M$ ,  $\Lambda$  is its dimensionless form, and  $G$  is Newton’s gravitational constant. For a given reference mass and a single posterior sample of  $(M_1, M_2, \Lambda_1, \Lambda_2)$ , we can solve equation (12) to get a unique  $\lambda_{\text{ref}}$ ,  $\lambda^1$ , and then  $\Lambda_{\text{ref}}$ . With a group of posterior samples of  $(M_1, M_2, \Lambda_1, \Lambda_2)$ , the distribution of  $\Lambda_{\text{ref}}$  can be inferred at this reference mass. After varying the reference mass in a given range and following the same procedure outlined above, we can get the corresponding constraints on dimensionless tidal deformability of NSs in this mass range (see the upper panel of Figure 4).

The NS’s tidal deformability  $\Lambda$  and dimensionless moment of inertia  $\bar{I} \equiv c^4 I/G^2 M^3$  are found to have an EoS-insensitive relation, which is the so-called I-Love relation, where  $I$  is the moment of inertia. Here we take the function form from Yagi & Yunes (2013), which reads

$$\log_{10} \bar{I} = \sum_{n=0}^4 a_n (\log_{10} \Lambda)^n, \quad (13)$$

where  $a_n$  are the fit coefficients, which are adopted from Landry & Kumar (2018). For a reference mass  $M_{\text{ref}}$ , a group of possible  $\Lambda_{\text{ref}}$  are calculated from equation (12) for each group of a posterior sample, then we can calculate a group of possible moment of inertia  $I$  from equation (13). After varying the reference mass, we get constraints on the moments of inertia (see middle panel of Figure 4).

The BE also have an EoS-insensitive relation with dimensionless tidal deformability  $\bar{I}$ , i.e.,

$$BE/M = \sum_{n=0}^4 b_n \bar{I}^{-n}. \quad (14)$$

Here we take the fit coefficients  $b_n$  from Steiner et al. (2016) and use equations (12–14) to calculate a sample of BE and its 90% range—for a given reference mass and a given posterior sample, then change reference mass and repeat the same procedure to set constraints on the whole mass range considered (see the lower panel of Figure 4).

### 3.2.2. Posterior choices and mass range



For our current purposes we adopt four posterior samples, including two obtained in this work (i.e., the Posterior Sample A corresponding to that of Test E and the Posterior Sample B for Test F) and the other two adopted from [Abbott et al. \(2018\)](#). The Posterior Sample C is available on the web<sup>7</sup>, which is the result of a universal relation-based analysis. The Posterior Sample D is taken from the same literature but it is the result of a spectral EOS parameterization analysis that imposes a maximum gravitational mass of at least  $1.97M_{\odot}$  ([Antoniadis et al. 2013](#)).

Here we focus on the NS masses between  $1.17 M_{\odot}$  and  $1.68 M_{\odot}$ , which cover the most probable mass range of galactic double NS systems. Please note that here we take the 68% lower (upper) limit of the lowest (highest) mass in 12 galactic double NS systems whose individual masses were accurately measured (see [Farrow et al. 2019](#), and the references therein).

### 3.2.3. Constraint results

The resulting  $\Lambda$ ,  $I$ , and BE in the mass range of galactic double neutron stars are summarized in Figure 4. We can see that the constraints in all the four scenarios are consistent with each other (see Table 5), giving the rather large uncertainties. However, there are some interesting general tendencies. Posterior Sample A and Posterior Sample D tend to favor higher  $\Lambda$  and  $I$ , but have a lower BE than the cases of Posterior Sample B and Posterior Sample C. Interestingly, similar conclusions about the difference of  $\Lambda_{1.4}$  in Posterior Sample C and Posterior Sample D were drawn in [Abbott et al. \(2018\)](#), who attributed the difference to the additional  $M_{\text{TOV}}$  constraint. Besides, although dimensionless tidal deformability decreases very quickly with the increasing reference mass (see Figure 4), the moment of inertia and the binding energy increase almost linearly with  $M_{\text{ref}}$ . In the meantime, the lower error is smaller than the upper error in all these cases. Additionally, because of the use of universal relations, the relative error of  $I$  is significantly smaller than that of  $\Lambda$ , and the relative error of BE is systematically smaller than that of  $I$ .

It is also evident from Figure 4 that the more constraints/data we add, the smaller relative error of the inferred global properties of galactic NSs we get. Posterior Sample D infers a smaller relative error of global properties than that of Posterior Sample C, because the former adopts an additional mass constraint  $M_{\text{TOV}} > 1.97M_{\odot}$ . Posterior Sample A adopts a tighter mass constraint  $2.5M_{\odot} > M_{\text{TOV}} > 2.06M_{\odot}$  and additional nuclear constraint than Posterior Sample D, so it gets smaller rel-

ative errors of  $\Lambda$ ,  $I$ , and BE than the latter. Interestingly, Posterior Sample B gets the smallest relative error because of the additional tighter mass constraint, and because the data of LMXB sources with burst are considered.

The canonical global properties of Posterior Samples A and B shown in table 5 are consistent with those of Test E and F shown in Table 4, because they adopt the same posterior sample, with the latter been directly reconstructed from posterior sample of EoS parameters  $\{\hat{p}_1, \hat{p}_2, \hat{p}_3, \hat{p}_4\}$  and the former being inferred from NS properties  $\{M_1, M_2, \Lambda_1, \Lambda_2\}$  of sources of GW170817 and universal relations.

## 4. DISCUSSION AND SUMMARY

We combine the gravitational-wave data, LMXB sources with thermonuclear bursts or nuclear constraints on the symmetry energy together to do the joint analysis, finding that different data sets can constrain different pressure parameters, i.e., the constraint on  $\hat{p}_1$  mainly comes from nuclear constraints, the constraint on  $\hat{p}_2$  is mainly contributed by the gravitational-wave data and the LMXB sources with thermonuclear bursts, the constraint on  $\hat{p}_3$  heavily relies on the LMXB source data and the current bounds of  $M_{\text{TOV}}$ , the range of  $\hat{p}_4$  can be slightly narrowed down by LMXB sources with thermonuclear bursts. We also find that nuclear constraints tend to give larger  $R_{1.4}$  and LMXB sources with thermonuclear bursts tend to indicate smaller ones. Our  $\Lambda_{1.4}$  bounds found in Test F are consistent with those of [Kumar, & Landry \(2019\)](#). However, our median value is a bit higher than that found in [Kumar, & Landry \(2019\)](#). Such a difference is likely caused by the very different analysis methods and by our additional bounds on  $M_{\text{TOV}}$ .

With some EoS-insensitive relations and our posterior samples, we have evaluated the possible ranges of tidal deformability, moment of inertia, and BE of NSs in the mass range of galactic double NS systems. The constraints in all the four scenarios are consistently (see Table 5) produce rather high uncertainties. Particularly, for the NS with a canonical mass of  $1.4M_{\odot}$ , we have  $I_{1.4} = 1.43_{-0.13}^{+0.30} \times 10^{38} \text{ kg} \cdot \text{m}^2$ ,  $\Lambda_{1.4} = 390_{-210}^{+280}$ ,  $R_{1.4} = 11.8_{-0.7}^{+1.2} \text{ km}$ , and  $BE_{1.4} = 0.16_{-0.02}^{+0.01} M_{\odot}$  if the constraints from the nuclear data and the gravitational-wave data have been considered together. For the joint analysis of gravitational-wave data and LMXB sources with thermonuclear bursts, we have  $I_{1.4} = 1.28_{-0.08}^{+0.15} \times 10^{38} \text{ kg} \cdot \text{m}^2$ ,  $\Lambda_{1.4} = 220_{-90}^{+90}$ ,  $R_{1.4} = 11.1_{-0.6}^{+0.7} \text{ km}$  and  $BE_{1.4} = 0.18_{-0.01}^{+0.01} M_{\odot}$ . These results suggest that the current constraints on  $\Lambda$  still suffer from significant systematic uncertainties (see also, e.g. [Lattimer & Lim](#)

<sup>7</sup> <https://dcc.ligo.org/LIGO-P1800115/public>

**Table 6.** 90% Interval of Gravitational-wave Detection Frame Parameters in Different Tests

Test / Parameter	$\mathcal{M}_c/M_\odot$	$t_c/s$	$q$	$\chi_{1z}$	$\chi_{2z}$	$\theta_{jn}/deg$
GW original	$1.1975^{+0.0001}_{-0.0001}$	$1187008882.4307^{+0.0008}_{-0.0005}$	$0.88^{+0.10}_{-0.14}$	$0.00^{+0.02}_{-0.01}$	$0.00^{+0.02}_{-0.02}$	$150^{+12}_{-9}$
Test A	$1.1975^{+0.0001}_{-0.0001}$	$1187008882.4307^{+0.0007}_{-0.0003}$	$0.90^{+0.09}_{-0.12}$	$0.00^{+0.02}_{-0.01}$	$0.00^{+0.02}_{-0.01}$	$151^{+13}_{-9}$
Test B	$1.1975^{+0.0001}_{-0.0001}$	$1187008882.4307^{+0.0007}_{-0.0003}$	$0.89^{+0.10}_{-0.13}$	$0.00^{+0.02}_{-0.01}$	$0.00^{+0.02}_{-0.01}$	$150^{+14}_{-9}$
Test C	$1.1975^{+0.0001}_{-0.0001}$	$1187008882.4286^{+0.0007}_{-0.0003}$	$0.87^{+0.11}_{-0.13}$	$0.00^{+0.02}_{-0.01}$	$0.00^{+0.02}_{-0.02}$	$148^{+12}_{-9}$
Test D	$1.1975^{+0.0001}_{-0.0001}$	$1187008882.4306^{+0.0006}_{-0.0002}$	$0.88^{+0.10}_{-0.12}$	$0.00^{+0.02}_{-0.01}$	$0.00^{+0.02}_{-0.01}$	$150^{+13}_{-9}$
Test E	$1.1976^{+0.0001}_{-0.0001}$	$1187008882.4308^{+0.0007}_{-0.0003}$	$0.90^{+0.08}_{-0.12}$	$0.00^{+0.02}_{-0.01}$	$0.00^{+0.02}_{-0.01}$	$151^{+12}_{-9}$
Test F	$1.1975^{+0.0001}_{-0.0001}$	$1187008882.4305^{+0.0003}_{-0.0002}$	$0.88^{+0.10}_{-0.10}$	$-0.00^{+0.01}_{-0.01}$	$-0.00^{+0.02}_{-0.01}$	$151^{+13}_{-9}$

Note. The unit of  $\theta_{jn}$  is transformed from rad to degree to compare with other analyses.

2013; Abbott et al. 2018), while  $I_{1.4}$  and  $BE_{1.4}$  are relatively better bounded.

We thank the anonymous referee for the helpful suggestions. This work was supported in part by NSFC under grants of No. 11525313 (i.e., Funds for Distinguished Young Scholars), No. 11433009 and No. 11773078, the Funds for Distinguished Young Scholars of Jiangsu Province (No. BK20180050), the Chinese Academy of

Sciences via the Strategic Priority Research Program (grant No. XDB23040000), and the Key Research Program of Frontier Sciences (No. QYZDJ-SSW-SYS024).

*Software:* Bilby (Ashton et al. 2019, version 0.5.5, ascl:1901.011, <https://git.ligo.org/lscsoft/bilby/>), PyCBC (ThePyCBCTeam2018, version 1.13.6, ascl:1805.030, <http://doi.org/10.5281/zenodo.3265452>), PyMultiNest (Buchner 2016, version 2.6, ascl:1606.005, <https://github.com/JohannesBuchner/PyMultiNest>).

## APPENDIX

### A. GRAVITATIONAL-WAVE PARAMETERS

To further check our results, we carry out another test labeled as ‘‘GW’’, which samples  $\{\mathcal{M}_c, q, \Lambda_1, \Lambda_2, \chi_1, \chi_2, \theta_{jn}, t_c, \Psi\}$ . We have also calculated the properties of gravitational-wave parameters (see Table 6 and Figure 5). Our results are self-consistent among all test scenarios and are in agreement with Abbott et al. (2019). We do not provide the property of polarization  $\Psi$ , because it is poorly constrained and carries little astrophysical information. The error of  $\theta_{jn}$  is reduced compared with that of Abbott et al. (2017a) but consistent with Abbott et al. (2019), because the sky location of GW170817 is fixed to its optical counterpart. The coalescence time  $t_c$  of Test C is slightly different from other tests because of the adoption of the TaylorF2 waveform model. In our analysis the ‘‘aligned spin prior’’ is assumed, which implies that the information in the direction that is perpendicular to the orbital angular momentum has been lost. In other words, we are simply constraining the spin in the  $z$  direction, for which a zero median value is expected (see also Abbott et al. 2019).

## REFERENCES

- Abbott, B. P., Abbott, R., Abbott, T. D., et al. 2017, *PhRvL*, 119, 161101
- Abbott, B. P., Abbott, R., Abbott, T. D., et al. 2017, *ApJL*, 848, L12
- Abbott, B. P., Abbott, R., Abbott, T. D., et al. 2018, *PhRvL*, 121, 161101
- Abbott, B. P., Abbott, R., Abbott, T. D., et al. 2019, *Physical Review X*, 9, 011001
- Abbott, B. P., Abbott, R., Abbott, T. D., et al. 2019, *Physical Review X*, 9, 031040
- Akmal, A., Pandharipande, V. R., & Ravenhall, D. G. 1998, *PhRvC*, 58, 1804
- Allen, B., Anderson, W. G., Brady, P. R., et al. 2012, *PhRvD*, 85, 122006
- Annala, E., Gorda, T., Kurkela, A., & Vuorinen, A. 2018, *PhRvL*, 120, 172703
- Antoniadis, J., Freire, P. C. C., Wex, N., et al. 2013, *Science*, 340, 448
- Ashton, G., Hübner, M., Lasky, P. D., et al. 2019, *Bilby: Bayesian inference library*, ascl:1901.011
- Baillot d’Etivaux, N., Guillot, S., Margueron, J., et al. 2019, arXiv:1905.01081
- Biwer, C. M., Capano, C. D., De, S., et al. 2019, *PASP*, 131, 024503

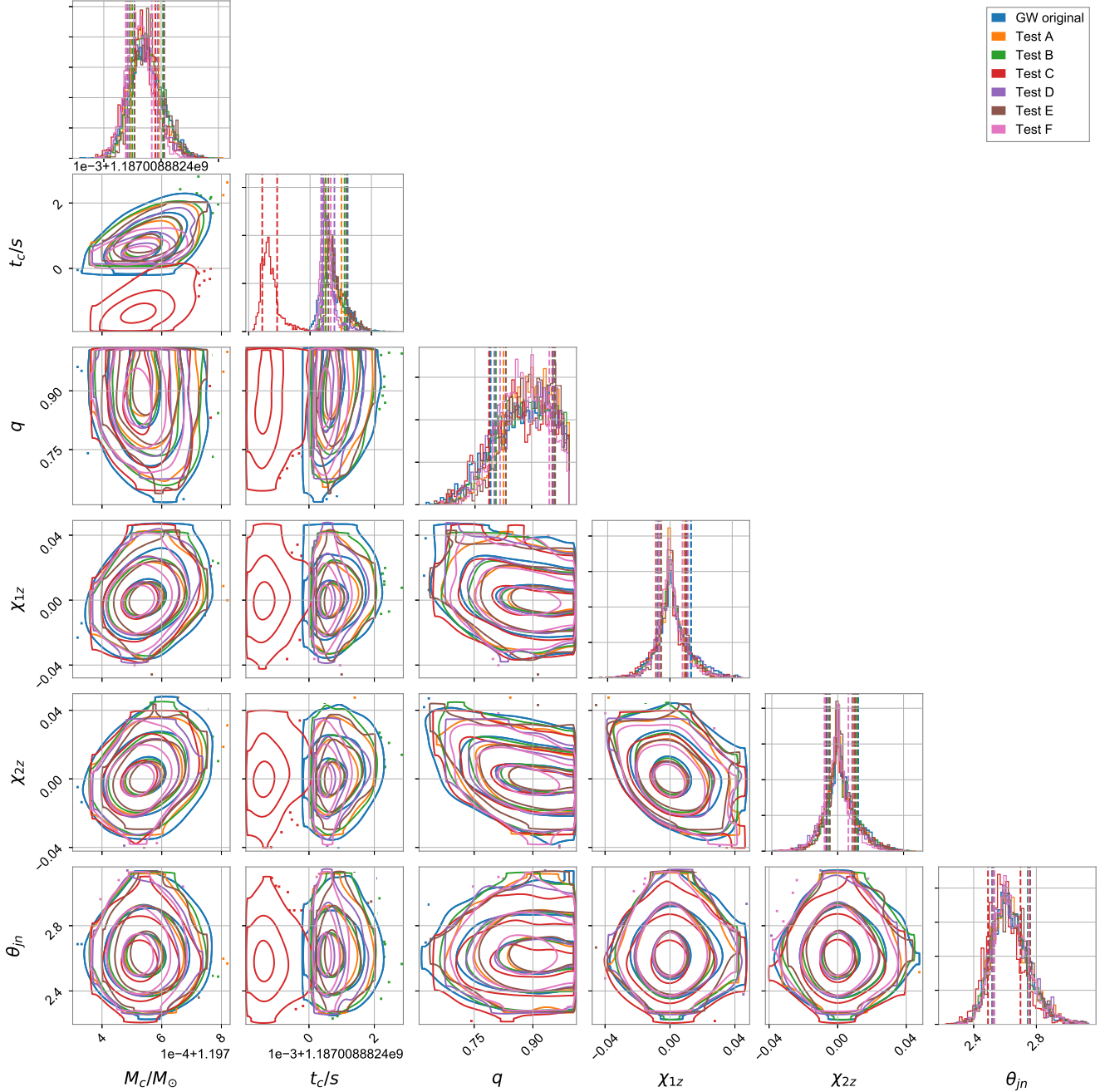


**Figure 5.** Posterior distribution of gravitational-wave parameters in each test.

Buchner, J. 2016, PyMultiNest: Python interface for MultiNest, ascl:1606.005  
 Breu, C., & Rezzolla, L., 2016, MNRAS, 459, 646  
 Cromartie, H. T., Fonseca, E., Ransom, S. M., et al. 2019, Nature Astronomy  
 De, S., Finstad, D., Lattimer, J. M., et al. 2018, PhRvL, 121, 091102  
 Del Pozzo, W., Li, T. G. F., Agathos, M., Van Den Broeck, C., & Vitale, S. 2013, PhRvL, 111, 071101

Demorest, P. B., Pennucci, T., Ransom, S. M., Roberts, M. S. E., & Hessels, J. W. T. 2010, Nature, 467, 1081  
 Fan, Y. Z., Wu, X. F., & Wei, D. M. 2013, PhRvD, 88, 067304  
 Farrow, N., Zhu, X.-J., & Thrane, E. 2019, ApJ, 876, 18  
 Fasano, M., Abdelsalhin, T., Maselli, A., & Ferrari, V. 2019, PhRvL, 123, 141101  
 Fattoyev, F. J., Piekarewicz, J., & Horowitz, C. J. 2018, PhRvL, 120, 172702

- Guillot, S., Servillat, M., Webb, N. A., & Rutledge, R. E. 2013, *ApJ*, 772, 7
- Kumar, B., & Landry, P. 2019, *PhRvD*, 99, 123026
- Kurkela, A., Fraga, E. S., Schaffner-Bielich, J., & Vuorinen, A. 2014, *ApJ*, 789, 127
- Krastev, P. G., & Li, B.-A. 2019, *Journal of Physics G Nuclear Physics*, 46, 074001
- Landry, P., & Kumar, B. 2018, *ApJL*, 868, L22
- Lattimer, J. M., & Prakash, M. 2001, *ApJ*, 550, 426
- Lattimer, J. M. 2012, *ARNPS*, 62, 485
- Lattimer, J. M., & Lim, Y. 2013, *ApJ*, 771, 51
- Lattimer, J. M., & Steiner, A. W. 2014, *EPJA*, 50, 40
- Lattimer, J. M., & Steiner, A. W. 2014, *ApJ*, 784, 123
- Lattimer, J. M., & Prakash, M. 2016, *PhR*, 621, 127
- Levan, A. J., Lyman, J. D., Tanvir, N. R., et al. 2017, *ApJL*, 848, L28
- Lim, Y., & Holt, J. W. 2018, *PhRvL*, 121, 062701
- Lim, Y., & Holt, J. W. 2019, *arXiv:1902.05502*
- Lindblom, L. 2010, *PhRvD*, 82, 103011
- Lindblom, L., & Indik, N. M. 2014, *PhRvD*, 89, 064003
- Ma, P.-X., Jiang, J.-L., Wang, H., et al. 2018, *ApJ*, 858, 74
- McNeil Forbes, M., Bose, S., Reddy, S., et al. 2019, *arXiv:1904.04233*
- Most, E. R., Weih, L. R., Rezzolla, L., & Schaffner-Bielich, J. 2018, *PhRvL*, 120, 261103
- Nättilä, J., Steiner, A. W., Kajava, J. J. E., Suleimanov, V. F., & Poutanen, J. 2016, *A&A*, 591, A25
- Oertel, M., Hempel, M., Klähn, T., & Typel, S. 2017, *RvMP*, 89, 015007
- Özel, F., & Psaltis, D. 2009, *PhRvD*, 80, 103003
- Özel, F., & Freire, P. 2016, *ARA&A*, 54, 401
- Özel, F., Psaltis, D., Güver, T., et al. 2016, *ApJ*, 820, 28
- Raithel, C. A., Özel, F., & Psaltis, D. 2017, *ApJ*, 844, 156
- Radice, D., & Dai, L. 2019, *EPJA*, 55, 50
- Read, J. S., Lackey, B. D., Owen, B. J., & Friedman, J. L. 2009, *PhRvD*, 79, 124032
- Read, J. S., Markakis, C., Shibata, M., et al. 2009, *PhRvD*, 79, 124033
- Steiner, A. W., Lattimer, J. M., & Brown, E. F. 2010, *ApJ*, 722, 33
- Steiner, A. W., Lattimer, J. M., & Brown, E. F. 2013, *ApJL*, 765, L5
- Steiner, A. W., Lattimer, J. M., & Brown, E. F. 2016, *EPJA*, 52, 18
- Tews, I., Lattimer, J. M., Ohnishi, A., & Kolomeitsev, E. E. 2017, *ApJ*, 848, 105
- The PyCBC Team 2018, *PyCBC: Gravitational-wave data analysis toolkit*, *ascl:1805.030*
- Yagi, K., & Yunes, N. 2013, *Sci*, 341, 365